Numerical simulation of viscous filament stretching flows

M.S. Chandio, H. Matallah and M.F. Webster
Department of Computer Science, Institute of non-Newtonian Fluid Mechanics, University of Wales Swansea, Swansea, UK

Received July 2002
Revised February 2003
Accepted April 2003

Keywords *Flow, Viscosity, Numerical analysis*

Abstract *A numerical study on the stretching of a Newtonian fluid filament is analysed. Stretching is performed between two retracting plates, moving under constant extension rate. A semi-implicit Taylor-Galerkin/pressure-correction finite element formulation is employed on variable-structure triangular meshes. Stability and accuracy of the scheme is maintained up to large Hencky-strain levels. A non-uniform radius profile, minimum at the filament mid-plane, is observed along the filament-length at all times. We have found maintenance of a suitable mesh aspect-ratio around the mid-plane region (maximum stretch zone) to restrict early filament break-up and consequently solution divergence. As such, true transient flow evolution is traced and the numerical results bear close agreement with the literature.*

1. Introduction

Flows with significant elongational components are common in industrial applications, such as in fibre spinning. The same applies within some rheological instruments, as typified under the measurement of extensional viscosity. The most common types of extensional flow instabilities that occur are necking, capillary and filament break-up. In fact, filament-stretching flows are common in everyday-life, and may be used as a technique to measure extensional viscosity in highly mobile fluids, where extension rates may be large. Currently, the filament stretching extensional rheometer (FSR) has emerged as a controllable device, for such purposes. Matta and Tytus (1990) were the first to introduce such a device. A modern form has been developed by Tirtaatmadja and Sridhar (1993) for low-viscosity liquids. In recent years, due to the development of filament stretching rheometers, attention has been diverted into this new area, and on to the measurement of extensional properties of polymer solutions and melts. Gaudet and McKinley (1998), Sizaire and Legat (1997), Yao and McKinley (1998) and Yao *et al.* (1998) have performed numerical simulations, based on the filament stretching rheometer of Tirtaatmadja and Sridhar. Experimental studies were reported in Spiegelberg and McKinley (1996), Spiegelberg *et al.* (1996) and Yao *et al.* (1998). Major attention has been focused on the analysis and comparison of the fluid kinematic and dynamic evolution of the extensional stresses in these liquid

International Journal of Numerical Methods for Heat & Fluid Flow
Vol. 13 No. 7, 2003
pp. 899-930

0961-5539
DOI 10.1108/09615530310502091

bridges. Both Newtonian and viscoelastic fluids have been considered. In the literature, little has been reported numerically, based on the FSR of Tirtaatmadja and Sridhar (1993). Numerical solutions have been restricted largely to small deformations (Yao and McKinley, 1998). In the present work, we discuss in some detail the numerical difficulties that arise during the simulation of elongation in liquid bridges. We consider the validity of these techniques whilst calculating extensional viscosity. First, a brief literature review is presented, covering the extensional deformation histories observed.

Matta and Tytus (1990) investigated constant force experiments, allowing the lower-plate, that grips the fluid, to fall under gravity. In such circumstances, these authors showed that the liquid bridge experienced constant uniform extension when the plates moved apart rapidly. Tirtaatmadja and Sridhar (1995) considered a variation to the stretching procedure for mobile polymer systems. In their work, the plates were moved apart at an exponential retraction-rate, so as to impose constant stretch-rate at the centre of the filament. Berg *et al.* (1995) were the first to conduct experimental tests on a reducing diameter device (RDD). The diameter of the end-plates, in such devices, is reduced at an exponential rate with filament elongation. This type of device exhibits homogeneous flow kinematics in the liquid bridge at low Hencky-strains ($\varepsilon = 1.4$). However, it has proved practically difficult to investigate the extensional properties of liquid bridges using the RDD, due to mechanical design constraints.

Yao and McKinley (1998) conducted a numerical study to investigate the transient response of Newtonian and viscoelastic liquid bridges. A commercial finite element package (POLYFLOW) was employed in their simulations, using nine-node quadratic, quadrilateral elements[1]. An elliptic mapping and remeshing technique (Thompson *et al.* (1985)) was introduced to redistribute the internal nodes, according to the displacement of the moving boundaries. This was found to be helpful in avoiding excessive mesh distortion. Their findings were based on the RDD by Berg *et al.* (1995) and a velocity compensation technique, as proposed by Tirtaatmadja and Sridhar (1993). The spatial and temporal non-homogeneity of the fluid kinematics and viscoelastic stress were investigated in some considerable detail. The transient response for Newtonian fluids was compared against that for some viscoelastic fluids. Yao and McKinley argue that accurate extensional material properties cannot be based on net experimental tensile force measurements, due to inherent inhomogeneity of deformation within the filament. A RDD approach is commended as being optimal to improve homogeneity in flow kinematics. Sizaire and Legat (1997) conducted a similar numerical study to that of Yao and McKinley (1998). Sizaire and Legat neglected the effects of gravity and inertia and reasonable agreement was reached in comparison to the literature. Indeed, the velocity compensation technique (Tirtaatmadja and Sridhar, 1993) may

simplify the calculation of extensional viscosity. In contrast, the stress field developed within the filament may remain far from homogeneous (Spiegelberg *et al.*, 1996).

Gaudet and McKinley (1996, 1998) numerically analysed the transient evolution of free-surface shape and applied force on the plates for Newtonian liquid bridges. In their work, the plates moved apart at a constant, prescribed velocity. Deformation patterns and liquid-bridge break-up time, for materials of different viscosities, were investigated using a boundary integral method. In their subsequent work, Gaudet and McKinley (1998) introduced a viscoelastic liquid-bridge to simulate the extensional dynamics of stretching filaments for constant viscosity Boger fluids. Such fluids were represented conveniently by Oldroyd-B type models. Predictions were compared for low Hencky-strains to their experimental results and found to lie in close agreement.

Further reference may be found in Kolte and Szabo (1999), who analysed the capillary thinning of filaments for Newtonian and viscoelastic fluids, both experimentally and numerically. Here, a new instrument design was introduced, the liquid filament rheometer (LFR). The top-plate of this new device was fixed and the bottom-plate was attached to a moving-bar. When released, the bar and the bottom-plate fall under gravity. Minimum filament radius was recorded directly, capturing visual images on videotape, to be compared against numerical predictions. Hassager *et al.* (1998) investigated the occurrence of ductile failure for Newtonian and viscoelastic fluid samples without surface tension. These authors employed a Lagrangian finite element procedure, and hence demonstrated that Newtonian liquid bridges do not show ductile failure in the absence of surface tension. However, a mixed response (stability and ductile failure) was gathered for viscoelastic fluids. In addition, Ainser *et al.* (2000) performed simulations for the extension of viscoelastic samples, under the weight of a falling body. Again, a Lagrangian finite element approach was applied with a multi-mode Phan-Thien/Tanner (PIT) model. The flow characteristics were found to be sensitive to variation in model parameters. To avoid excess mesh distortion at protracted extension lengths, periodically these authors regenerated a fresh mesh (involving solution re-projection). A similar strategy is implemented in our own present studies.

Here, a semi-implicit Taylor-Galerkin/pressure-correction (SITpak) finite element method (Hawken *et al.*, 1990; Townsend and Webster, 1987) is used for the first time to model the stretching and break-up of Newtonian liquid bridges. We have appealed to the material parameters proposed by Sizaire and Legat (1997), identified by McKinley on the basis of steady-shear data, (Table I). Principal interest lies in quantifying solution evolution through various Hencky-strains (thus, through time). Plates are retracted at an exponential rate, to provide a constant stretch-rate at the filament mid-plane. The present work presumes axi-symmetry, and symmetry about the horizontal mid-plane between the flat-plates. Elsewhere, when considering viscoelastic fluids, we

have found it an effective strategy to take the full filament length, hence avoiding excessive discretisation errors about the filament mid-plane. This is particularly important in the viscoelastic counterpart problem, as there flow kinematics and stress enters the problem in a direct manner. Both influences of inertia and gravity may be neglected. The complexity of the problem lies in the dominating presence of deforming free-surface boundaries. To determine the eventual position of the free-surface, both dynamic and kinematic conditions must be imposed on such boundaries.

Our approach has been to hone the proposed pressure-correction fractional-staged algorithms (see Section 6) to demonstrate accuracy, stability and consistency, throughout this transient stretching problem. In particular, we have relied upon a direct approach instead of a compensation technique. The magnitude of the resultant strain-rates is observed at the filament mid-plane, as a function of Hencky-strain. Flow kinematics, resultant force on the plate, and extensional viscosity are each computed and compared against the literature. In this regard, we have recourse to refer extensively to the fundamental work of Sizaire and Legat (1997) and Yao and McKinley (1998). To avoid temporal mesh distortion and to maintain smooth and consistent nodal distribution, an efficient *remeshing algorithm* is invoked at each time-step.

2. Governing equations and field discretisation

For incompressible, isothermal laminar flows, the governing equations may be described through the system comprising of momentum and continuity equations. In the absence of body forces, these may be expressed in the form

$$\rho \frac{\partial u}{\partial t} = \nabla \cdot \mathbf{T} - \rho u \cdot \nabla u - \nabla p \tag{1}$$

$$\nabla \cdot u = 0 \tag{2}$$

where independent variables are time t, and space x. Dependent field variables are fluid velocity $u(x, t)$, and isotropic pressure, p. Material density is ρ. For Newtonian flows, the stress $\mathbf{T}$ is defined via a Newtonian viscosity μ_0, and the rate-of-deformation tensor D, and velocity gradient L, as

ρ (density)	890 ($\mathrm{kg\,m^{-3}}$)
$\dot{\varepsilon}_0$ (stretch-rate)	1.6 ($\mathrm{s^{-1}}$)
L_0 (initial lengh)	2.0×10^{-3} (m)
R_0 (initial radius)	3.5×10^{-3} (m)
χ (surface-tension coefficient)	28.9×10^{-3} (m)
μ_0(Newtonian shear viscosity)	98 (Pa s)

Table I.
Sample material properties

$$\mathbf{T} = 2\mu_0 D \tag{3}$$

where

$$D = \frac{L + L^t}{2} \quad \text{and} \quad L^t = \nabla u. \tag{4}$$

With a constant viscosity μ_0 and using the continuity equation (2), the celebrated Navier-Stokes equation can be recovered:

$$\rho \frac{\partial u}{\partial t} = \mu_0 \nabla^2 u - \rho u \cdot \nabla u - \nabla p \tag{5}$$

where $\mu_0 \nabla^2 u$ is the diffusion term.

For the dimensionless variables x^*, u^*, t^*, and p^*, we have chosen to scale by $x = x^* L_0,\ u = \dot{\varepsilon}_0 L_0 u^*,\ t = t^*/\dot{\varepsilon}_0,\ p = p^* \mu_0 \dot{\varepsilon}_0$, where L_0 is the initial length of the fluid filament and $\dot{\varepsilon}_0$ is the initial imposed stretch-rate. Hence, we may define an equivalent non-dimensional system of equations to (1) and (2) discarding the * notation for convenience of representation,

$$\mathrm{Re} \frac{\partial u}{\partial t} = \nabla^2 u - \mathrm{Re} u \cdot \nabla u - \nabla p, \quad \nabla \cdot u = 0 \tag{6}$$

where the non-dimensional group Reynolds number is defined as $\mathrm{Re} = \rho \dot{\varepsilon}_0 L_0^2 / \mu_0$.

A time-dependent SITpak algorithm (Hawken *et al.*, 1990; Townsend and Webster, 1987) is used to solve the governing equation (6). This involves a two-step Lax-Wendroff approach, based on a Taylor series expansion up to second order in time, to compute solutions through a time stepping procedure. A two-step pressure-correction method is applied to handle the incompressibility constraint. Employing a Crank-Nicolson treatment on diffusion terms produces an equation system of three fractional-staged equations. In stage one, a non-solenoidal velocity field $u^{(n+1/2)}$ and u^* are computed via a predictor-corrector doublet. The resulting mass-matrix bound equation is solved via Jacobi iteration. With the use of u^*, the second stage computes the pressure difference, $p^{n+1} - p^n$, via a Poisson equation, and the application of a direct Choleski solver. The third stage completes the time-step loop, calculating the end-of-time-step solenoidal velocity field u^{n+1}, again by a Jacobi iterative solver. The details upon this implementation may be found in Hawken *et al.* (1990) and Townsend and Webster (1987).

The velocity and pressure fields are approximated by $U(x,t) = U^j(t)\phi_j(x)$ and $P(x,t) = P^k(t)\psi_k(x)$, where U and P represent the vectors of nodal values of velocity and pressure, respectively, and ϕ_j are piecewise quadratic and ψ_k linear basis functions. The fully-discrete SITpak system of equations may be expressed in matrix form as,

$$\text{Stage 1a}\quad \left(\frac{2\text{Re}}{\Delta t}M+\frac{1}{2}S\right)\left(U^{n+\frac{1}{2}}-U^{n}\right)=\{-[S+\text{Re}N(U)]U+L^{\text{T}}P+F\}^{n}$$

$$\text{Stage 1b}\quad \left(\frac{\text{Re}}{\Delta t}M+\frac{1}{2}S\right)(U^{*}-U^{n})=\{-[S+\text{Re}N(U)]U+F\}^{n+\frac{1}{2}}+L^{\text{T}}P^{n} \tag{7}$$

$$\text{Stage 2}\quad K(P^{n+1}-P^{n})=-\frac{2\text{Re}}{\Delta t}LU^{*}$$

$$\text{Stage 3}\quad \frac{\text{Re}}{\Delta t}M(U^{n+1}-U^{*})=\frac{1}{2}L^{\text{T}}(P^{n+1}-P^{n}),$$

where M, S, $N(U)$, L, and K are consistent mass matrix, momentum diffusion matrix, convection matrix, pressure gradient matrix and pressure stiffness matrix, respectively. With elemental fluid area $\mathrm{d}\Omega$, such matrix notation implies,

$$M_{ij}=\int_{\Omega}\phi_i\phi_j\,\mathrm{d}\Omega,\quad N(U)_{ij}=\int_{\Omega}\phi_i\left(\phi_1U_1\frac{\partial\phi_j}{\partial x}+\phi_1U_1\frac{\partial\phi_j}{\partial y}\right)\mathrm{d}\Omega,$$

$$(L_k)_{ij}=\int_{\Omega}\frac{\partial\phi_j}{\partial x_k}\,\mathrm{d}\Omega,\quad K_{ij}=\int_{\Omega}\nabla\psi_i\nabla\psi_j\,\mathrm{d}\Omega,\quad S_{ij}=\int_{\Omega}\nabla\phi_i\nabla\phi_j\,\mathrm{d}\Omega, \tag{8}$$

$$F_i=\int_{\Gamma 2}g_2\phi_i\,\mathrm{d}\Gamma_2.$$

Next we proceed to specify the various aspects of the particular flow problem in question.

3. Problem description

We consider the case of a cylindrical filament of Newtonian fluid, stretched in time from a rest state (Figure 1). This procedure is termed "filament-stretching", and is of interest in several manufacturing processes,

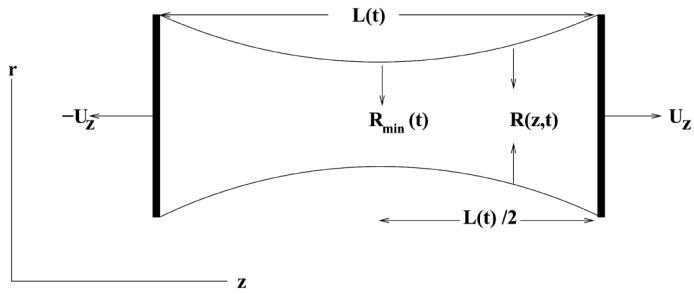

Figure 1.
Domain of filament sample

in particular, within the printing and food processing industries. This problem has been the object of numerous experimental and numerical investigations (Ainser *et al.*, 2000; Berg *et al.*, 1995; Gaudet and McKinley, 1996, 1998; Hassager *et al.*, 1998; Khan and Larson, 1987; Kolte and Szabo, 1999; Kröger *et al.*, 1992; Matta and Tytus, 1990; Padmanabhan, 1995; Sizaire and Legat, 1997; Spiegelberg and McKinley, 1996; Spiegelberg *et al.*, 1996; Tirtaatmadja and Sridhar, 1993, 1995; Tripathi *et al.*, 2000; Yao and McKinley, 1998; Yao *et al.*, 1998), as discussed above, and provides a wealth of data for comparison purposes.

In an ideal, homogeneous uniaxial elongational flow, a liquid bridge of initial length L_0 is stretched at an exponential rate, so that the filament length (similarly, distance separating any two material elements), at any particular time t, is given by:

$$L_t = L_0 \exp(\dot{\varepsilon}_0 t), \tag{9}$$

where $\dot{\varepsilon}_0$ is an imposed initial stretch-rate. In this ideal state and at any moment in time, the radius of the filament remains uniform throughout its length, and decreases from its initial value following the functional representation,

$$R_t = R_0 \exp\left(-\frac{\dot{\varepsilon}_0 t}{2}\right). \tag{10}$$

For pure-extensional uniaxial flows, the axial and radial velocity components are described, viz:

$$U_z = \dot{\varepsilon}_0 z \quad \text{and} \quad U_r = -\frac{1}{2}\dot{\varepsilon}_0 r. \tag{11}$$

The extensional viscosity μ_e, is defined via the tensile-stress growth in the fluid, as a function of the imposed-extension rate in the liquid bridge. This may be expressed in the form

$$\mu_e(\dot{\varepsilon}_0, t) = \frac{\tau_{zz} - \tau_{rr}}{\dot{\varepsilon}_0}, \tag{12}$$

where τ_{zz} and τ_{rr} are the normal components of extra-stress τ, defined as

$$\tau = \tau_s + \tau_p \tag{13}$$

Here, τ_s and τ_p are solvent and polymeric contributions to the extra-stress, respectively. For Newtonian flows, we have simply,

$$\tau = \tau_s = 2\mu_0 D. \tag{14}$$

For a Newtonian fluid with steady shear-viscosity μ_0, extensional viscosity can be represented as $\mu_e = 3\mu_0$ (Barnes *et al.*, 1989). In the absence of gravity and

inertia, the tensile-force acting on any cross-sectional filament of uniform radius R, can be obtained by integrating the normal stress differences $(\tau_{zz} - \tau_{rr})$, over that area. Thus, over the circular area of the plate, this leads to the identity,

$$F = \pi R^2(\tau_{zz} - \tau_{rr}). \tag{15}$$

Hence, via equation (12), the extensional viscosity can be expressed in terms of the applied normal force,

$$\mu_e(\dot{\varepsilon}_0) = \frac{F}{\pi R^2 \dot{\varepsilon}_0}. \tag{16}$$

As a consequence, the transient Trouton ratio (Tr) can be realised, through the ratio of extensional to steady shear-viscosity,

$$\mathrm{Tr} = \frac{\mu_e}{\mu_0}. \tag{17}$$

In the present study, we restrict attention to Newtonian fluids, and the set of operating conditions recorded in Sizaire and Legat (1997) (Table I). We recognize that the flow generated in the filament stretching configuration, as shown in (Figure 1), is neither ideal nor uniaxial, due to boundary influence. Here, we attempt to reproduce uniaxial elongation by separating end-plates at a prescribed increasing velocity. The main interest lies in Hencky-strain, $\varepsilon = \dot{\varepsilon}_0 t = \ln[L(t)/L_0]$, as a function of time, where $L(t)$ is the length of the whole filament (distance between the two plates) at time t, and $L_0 = L(0)$ is the initial sample length. Plates are retracted at an exponential-rate, by arranging

$$L(t) = \frac{L_0}{2}\exp(\dot{\varepsilon}_0 t). \tag{18}$$

The geometry (one quarter of domain) and the boundary conditions are provided in Figure 2. On the moving-plate, a driving velocity is imposed of:

$$U_z(t) = \frac{\dot{\varepsilon}_0 L_0}{2}\exp(\dot{\varepsilon}_0 t), \quad U_r(t) = 0. \tag{19}$$

The presence of non-deforming rigid end-plates and no-slip boundary conditions induces an additional shear-component to the flow, that develops locally to the end-plates. This will subsequently contribute to the deformation history.

4. Free-surface computation and boundary conditions

A complete definition of the problem requires appropriate boundary conditions. Dirichlet type boundary conditions are imposed on the known parts of the boundary. Continuity of normal and tangential velocities is applied at a

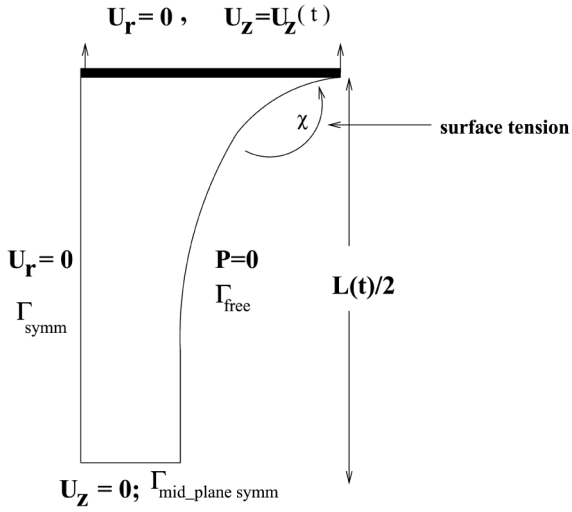

Figure 2.
Quarter geometry with boundary conditions

fluid-solid interface and continuity of stress at a free-surface (Frederiksen and Watts, 1981) (Figure 3). On the free boundary Γ_{fs}, considering an appropriate amount of surface-tension, we impose the following dynamic and kinematic boundary conditions, viz.

$$\sigma \cdot \mathbf{n} = -\left(p_{ext} + \chi\left(R_1^{-1} + R_2^{-1}\right)\right) \cdot \mathbf{n} \tag{20}$$

for the *dynamic boundary condition*, where σ is the Newtonian Cauchy-stress tensor,

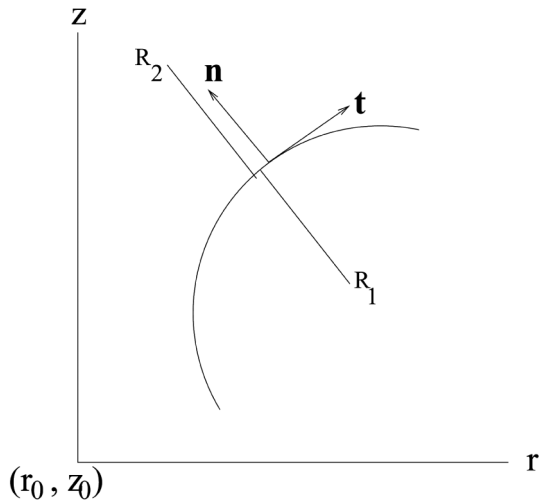

Figure 3.
Free-surface coordinate system

$$\sigma_{ij} = -(p\delta_{ij} + 2\mu_0 d_{ij}). \tag{21}$$

Here, χ, $\mathbf{n}$, $\mathbf{d}$ and p_{ext} are the surface tension coefficient, outward unit normal vector to the boundary $\partial\Gamma_{\text{fs}}$ rate-of-deformation tensor and atmospheric pressure, respectively. R_1 and R_2 are the principal radii of curvature of the interface, defined functionally (Keunings, 1986; Tanguy *et al.*, 1984) as,

$$R_1 = \left[\frac{1 + \left(\partial h/\partial z\right)^2}{\partial^2 h/\partial z^2}\right]^{3/2}, \quad R_2 = -h\left[1 + \left(\frac{\partial h}{\partial z}\right)^2\right]^{1/2} \tag{22}$$

with $h(z, t)$ as below. In the axisymmetric case, we must consider two radii of curvature, in planes orthogonal to each other.

For the *kinematic boundary condition*, and in order to find the eventual position of the free-surface, $h(z, t)$ we employ

$$\frac{\partial h}{\partial t} = u_r - u_z \frac{\partial h}{\partial z}, \quad \forall t. \tag{23}$$

If the free-surface is flat (vertical and normal to the horizontal), at the outset of the simulation, it will be driven by radial-velocity alone. This is always the case near the filament mid-plane, where we have,

$$\frac{\partial h}{\partial z} = 0, \quad \frac{\partial h}{\partial t} = u_r. \tag{24}$$

Elsewhere, equation (23) applies.

Due to the underpinning boundary conditions at the interface of the rigid end-plate and free-surface, the second term on the right of equation (23) stimulates instabilities on the free-surface (oscillations in profile, prominent in the first few elements, near the moving-plate) (Figure 4). Since these instabilities are local to the plate and free-surface region, a Crank-Nicolson treatment (with $\theta = 0.5$) is introduced in discretising this second-term, to the right of equation (23). With $\theta = 1$, equation (23) is recovered, under an explicit, one-backstep interpretation between t^{n+1} and t^n This is a measure taken to circumvent such numerical shortcomings, implemented as

$$\frac{\partial h^{t^{n+1}}}{\partial t} = u_r^t - u_z^t\left[\left(\frac{\partial h}{\partial z}\right)^{t^{n+1}} + \theta\left\{\left(\frac{\partial h}{\partial z}\right)^{t^n} - \left(\frac{\partial h}{\partial z}\right)^{t^{n-1}}\right\}\right] \tag{25}$$

where $0 \leq \theta \leq 1$. The use of equation (25) introduces smoothness and consistency in surface profiles (Figure 5), at no serious additional run-time cost. This avoids having to appeal to additional strategies to correct for free-surface instabilities. Satisfaction of filament volume conservation is ensured at each Hencky-strain time, through step 6 of our proposed algorithm (see Section 6).

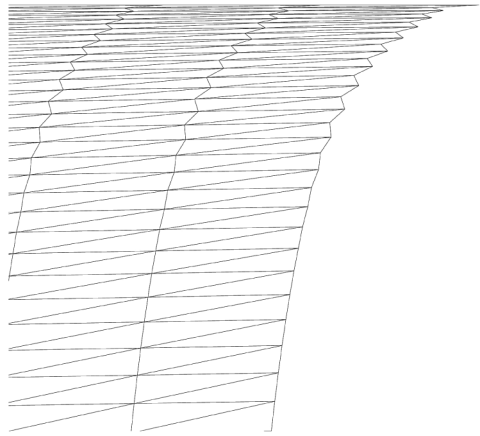

Figure 4.
Free-surface profile with instabilities

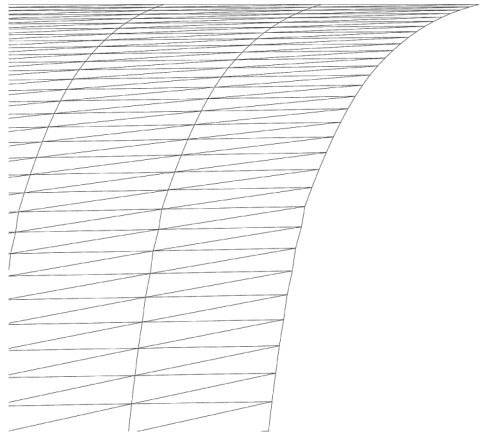

Figure 5.
Amended free-surface profile

5. Remeshing strategies

The choice of mesh is a crucial and important step in simulating any flow problem. Successful implementation of the numerical algorithm will depend in part upon the accuracy afforded by the mesh. It is conspicuous that the initial mesh will deform axially, in time, due to axial stretching and radially due to the pinning boundary conditions and the presence of the free-surface. In order to avoid mesh distortion, a strong remeshing rule [2] is needed to distribute the internal, as well as the boundary nodes, in such a fashion so as to maintain solution smoothness and stability up to higher levels of Hencky-strain. Two different methods are commonly employed to achieve this goal:

(1) a fixed-connectivity approach; and

(2) an automatic (adaptive)-mesh generation.

The fixed-connectivity approach will maintain the original sparsity pattern, associated with the matrices of the discrete equations. Distribution of interior nodes is made by a predetermined rule, using logarithmic, tan-hyperbolic (tanh), or uniform remeshing transformations. A second approach, used in recent years, is automatic mesh regeneration, particularly suitable for domains of arbitrary shape. This is achieved either by removing or inserting new elements until the mesh has acquired the desired nodal density in each region of the domain. Such an approach is most useful when the problem domain is significantly changed, due to large surface-tension effects. At relatively small deformation, the cost of generating new elements/nodes is low. However, under large deformation, as presently, this scheme is not cost-effective. It necessitates a full restart of any time-integration scheme involved, incurring large expense. The projection of solution (interpolation of primitive variables) implies considerable cost and introduces degradation in accuracy. To circumvent such difficulties, we have allotted to employ a fixed-connectivity approach. A fresh mesh is generated periodically in time (specific Hencky-strains, equating to excessive mesh distortion) and the solution is reprojected from the previous mesh to the new mesh. With a single mesh (Ml), we are able to retain stability up to Hencky-strain levels of 4.8^{+}. Nevertheless, a new mesh (M2) is deemed necessary at Hencky-strain $\varepsilon = 2.56$ to capture accuracy on the field, up to higher Hencky-strain levels of ($\varepsilon = 3.52^{+}$). Each of them is discussed in subsequent sections.

The kinematic iteration is a natural, separate solution stage for transient free-surface problems. From some initial flow field and domain, the free-surface and moving-boundary are advanced, according to the flow on such boundaries. An updated flow field is calculated and the boundaries advance again, consecutively. At each step, the mesh is adjusted so as to comply with the kinematic conditions (equation (25)) that match the motion of the moving boundaries to the velocity field. The kinematic iteration can be applied to solve a fully transient problem, or simply to solve a steady state problem. Due to the underpinning boundary conditions and the presence of the free-surface, the mesh experiences large deformation both radially (near the interface of the free-surface and the top-plate) and axially. Uniform remeshing is performed radially. For axial remeshing, where the mesh undergoes large stretching, two different remeshing techniques, tan-hyperbolic (tanh) and logarithmic remeshing rules have been implemented. The principal objective is to maintain smoothness of the mesh, in such a manner, that the nodes remain concentrated in certain regions of reference. Redistribution of mesh points and mesh concentration in the tanh-scheme are maintained by a specified control parameter (for more details, the reader is referred to the implementation of elliptic-mappings in Thompson *et al.*, 1985). A typical mapping function may be expressed as:

$$H_i^{t^{n+1}} = 1 - \frac{\tanh\left(\beta\left(1 - H_i^{t^n}\right)\right)}{\tanh\beta}, \tag{26}$$

where H_i, $0 \leq H_i \leq 1$, is the axial node-position of node i, and β is a mesh-density control parameter.

With the tanh-scheme, large aspect-ratios have resulted about the mesh mid-plane region. This causes filament break-up away from the mid-plane, at large Hencky-strain levels (Figure 6). Nevertheless, this scheme performs well at relatively small Hencky-strain levels. Since the problem under consideration, does experience large deformation, a log-remeshing algorithm is employed

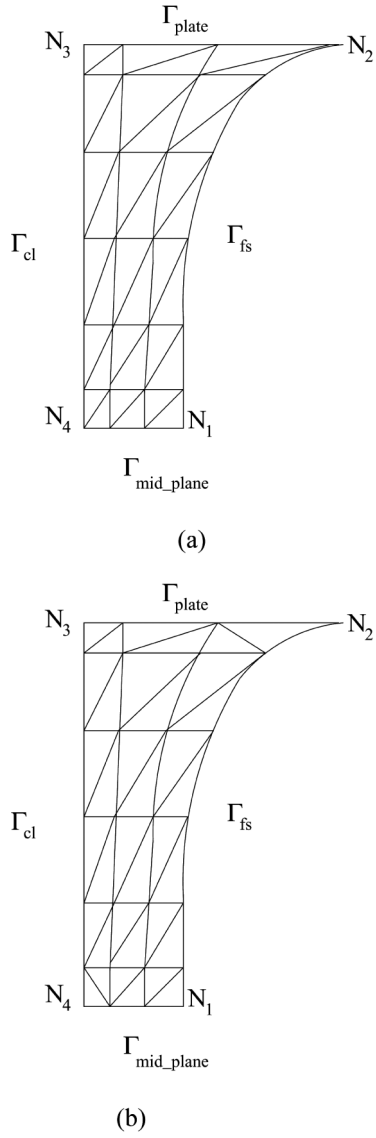

Figure 6.
Evolution of filament structure, Newtonian fluid, different Hencky-strains, tanh-remeshing scheme; arrows indicate minimum radial location

instead (Thompson *et al.*, 1985). Since the shape of the free-surface is highly curved near the top moving-plate, a finer mesh is deemed necessary to retain mesh aspect-ratio, and hence accuracy and stability. A modified log-remeshing approach is implemented for axial remeshing, where the mesh undergoes large stretching. This mapping function is given by

$$H_i^{t^{n+1}} = H_i^{t^n} + \frac{2i\Delta H_i^{t^{n+1}}}{\text{telm}(\text{telm}+1)}, \tag{27}$$

where telm is the total number of elements along the mesh-length, and $H_i^{t^{n+1}}$ is the current displacement. In this manner and by design, high element-density is maintained near the top-plate, see contrast in results between Figures 6 and 7.

Two rectangular meshes M1 of 12×40 elements, with 2,025 nodes and 960 triangular elements, and M2 of 12×106 elements, consisting of 5,025 nodes and 2,544 triangular elements, are used to perform the numerical simulation. The simulation commences from a simple mesh, but soon encounters large deformation that persists in time due to the transient nature of the problem. To avoid excessive mesh distortion at large deformation, and to retain smooth internal node distribution, the above cited low-cost remeshing algorithm (27) is applied at each time-step. Results are compared with Gaudet and McKinley (1998), Sizaire and Legat (1997) and Yao and McKinley (1998). Our solutions prove stable up to large Hencky-strains of 4.8^+ units. A high level of field solution accuracy is maintained and reported, up to Hencky-strains of 3.52^+ units. This exceeds findings in the literature.

With respect to mesh-structure, it has been found advantageous to introduce a slight modification in the corner elements of these meshes. In Figure 8(a), a schematic diagram of the initial mesh-orientation is shown. Here, node N_2 and N_4 are surrounded by two elements. In order to compute the velocity gradients at node N_i, we have recourse to a direct recovery technique (Matallah, 1998), which takes the average of nodal gradient values from the surrounding elements. This leads to quadratic continuous interpolation for gradients.

For an incompressible fluid, from the no-slip boundary conditions and continuity equation, we have $D_{rr} = D_{zz} = 0$ on end-plates. Through application of the recovery technique, corner-nodes N_2 and N_4, as shown in Figure 8(a), would gather contributions from more than one boundary element, To avoid this, we can use either a pointwise finite-difference approach on the boundaries, or adjust the element topology in that region, so that, only a single element contributes to the node. Note that nodes N_1 and N_3 receive contributions from a single element only. In the present simulations, we have allotted for mesh-orientation, as shown in Figure 8(b), with the use of one-dimensional point-wise approximation [3] over straight-line boundaries, Γ_{plate}, Γ_{cl} and $\Gamma_{\text{mid-plane}}$ (Figure 8(b)). We have found that point-wise approximation on the free-surface boundary (Γ_{fs}) performs less well. Hence, we have taken recovered velocity-gradients, upon the deformed

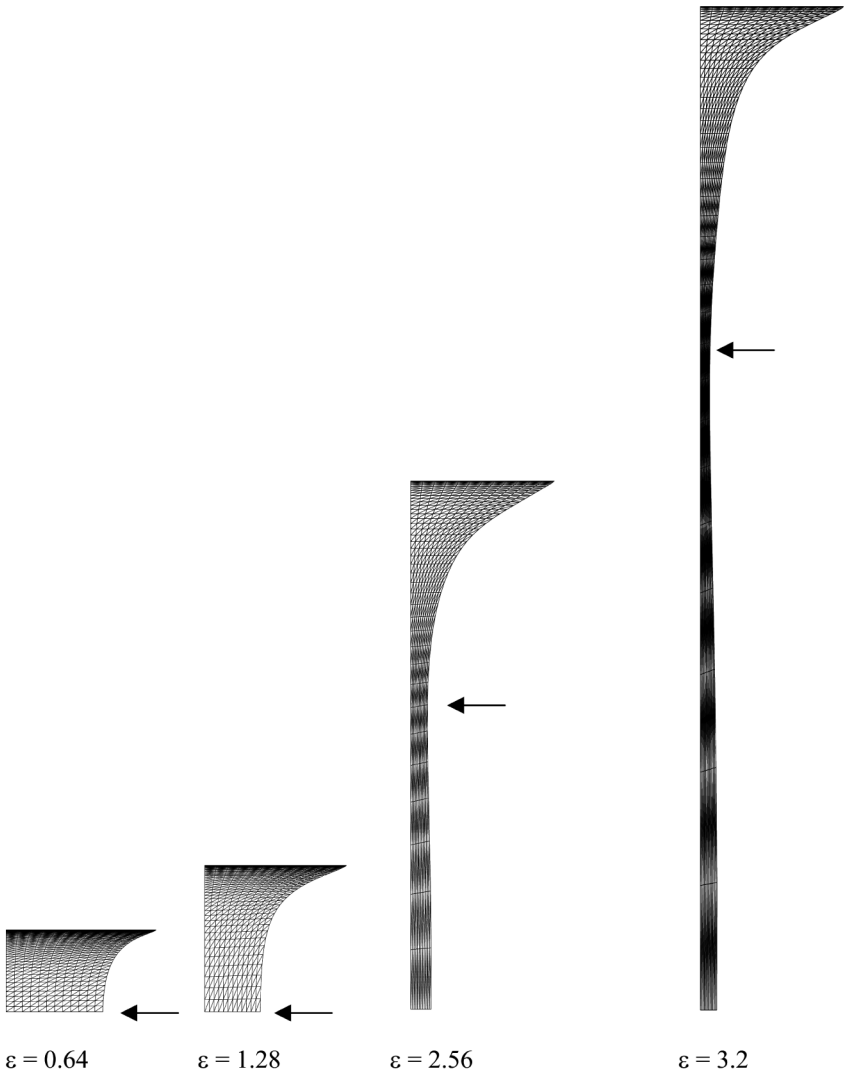

Figure 7.
Evolution of filament structure, Newtonian fluid, different Hencky-strains, modified log-remeshing scheme

free-surface boundary and internal field. Within the purely viscous scenario, the rate-of-deformation tensor only enters the calculation through a post-processing operation. However, for complex free-surface viscoelastic flows, where gradients play an important role in the calculation of primary-variable stress fields, the precise details on velocity gradient estimation are crucial. Both mesh-structure and velocity-gradient estimation must be revisited.

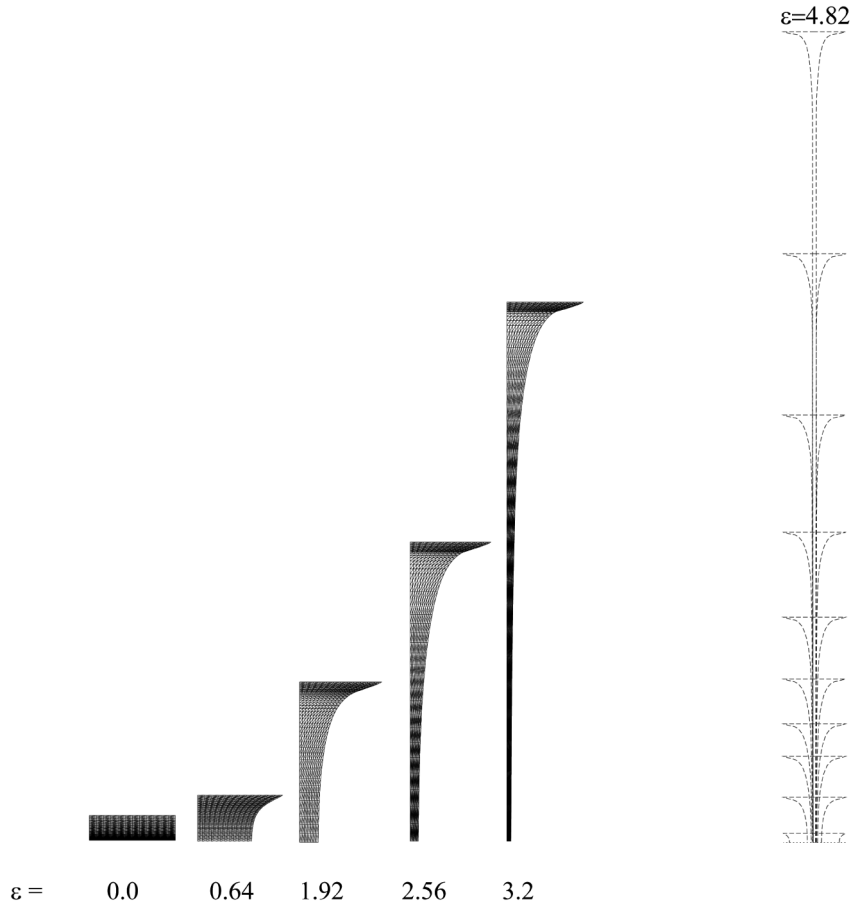

Figure 8.
Schematic diagram of mesh. (a) Initial, and (b) modified element orientation; corner nodes N_2 and N_4

6. Algorithm

The individual sequence of steps taken within a single Hencky-strain step (Δt_{Hencky}) are identified as follows:

(1) Hencky-strain, time-step number: $n\text{step} = n\text{step} + 1$.

(2) Fix plate-boundary conditions via equation (19).

(3) Move plate via equation (18) (Δt_{Hencky}).

(4) Update mesh-points locations, to occupy new position relative to plate-movement, via equation (27).

(5) Correct velocity and pressure fields solving fractional-stages (7), with dynamic boundary condition (20), to reach convergence tolerance 10^{-5}, (Δt_{inner}).

(6) Compute free-surface via equation (25), (Δt_{fs})

- update mesh-points radially;
- compute filament volume if $\|\mathrm{Vol}^{\mathrm{exact}} - \mathrm{Vol}^{h}\|/\|\mathrm{Vol}^{\mathrm{exact}}\| \leq \mathrm{Vol}^{\mathrm{tol}}$ go to 8, continue;
- solve fractional-stages (7) to update-solution;
- Go to 7.

(7) Print output: normal force, extension-rate, Trouton ratio, $R_{\mathrm{min.}}$

(8) Print solution at current Hencky-strain level (real-time).

(9) Go to 2.

In the current formulation, we choose three different time-step sizes as $\Delta t_{\mathrm{Hencky}}$ to shift the plate at each Hencky-strain (real-time, step 3), $\Delta t_{\mathrm{inner}}$ to compute the velocity field (step 5) and Δt_{fs}, for free-surface movement. For mesh Ml, up to Hencky-strain levels $\varepsilon = 2.56$, we have taken $\Delta t_{\mathrm{Hencky}} = \Delta t_{\mathrm{inner}}$. For mesh M2, at smaller mesh-size, we have used $\Delta t_{\mathrm{inner}} = \Delta t_{\mathrm{Hencky}} \times 0.5$ and for free-surface computation, taken $\Delta t_{\mathrm{fs}} = \Delta t_{\mathrm{inner}} \times 0.5$.

Since the flow under consideration is incompressible, the volume of the liquid-bridge should remain constant throughout the stretching period. This condition is met at step 6 of the algorithm. At each Δt_{fs}, the free-surface boundary is shifted via equation (25). This is accomplished in such a fashion that the relative error norm between the exact volume ($\mathrm{Vol}^{\mathrm{exact}}$, initial volume) and the computed instantaneous volume (Vol^{h}) remains less than the specified tolerance ($\mathrm{Vol}^{\mathrm{tol}}$), taken here as 1 per cent.

7. Numerical results and discussion

A half-length model (Figure 2), is considered for simulation at a negligible Reynolds number. The volume of the liquid bridge is conserved at all times. The deformation of the filament and its free-surface evolution is shown in Figure 7, at various Hencky-strain (time) levels. The radius varies along the filament length at all times, due to the underpinning boundary conditions on the moving end-plate. Yet, minimum radial location should always correspond to the mid-plane of the filament. Large deformation is observed during stretching. Computed minimum filament radius is plotted against time in Figure 9. The slope of this variation in minimum radius R_{min}, is observed to decrease in a smooth exponential fashion (equation (10)), up to a Hencky-strain level of $\varepsilon = 2.0$. Subsequently upon mesh Ml, a slight departure is observed that continues up to the point of filament break-up ($\varepsilon = 4.8^{+}$). Though an acceptable minimum radius profile is achieved up to Hencky-strain level of $\varepsilon = 4.8^{+}$, still this setting failed to capture accuracy in field variables of interest. For example, in flow kinematics, strain-rates and extensional viscosity distributions. This is due to high deformation in the middle of the fluid column, where mesh elements acquire large aspect ratios. Hence, a new mesh (M2) was

generated and simulation recommenced, by solution reprojection from mesh Ml at $\varepsilon = 2.56^{+}$. With this new mesh, we have been able to recapture accuracy on the field to relatively large levels of Hencky-strain. As demonstrated in Figure 9, the filament thins rapidly at the symmetry plane for Hencky-strains of $\varepsilon = 3.2^{+}$. This trend subsequently causes filament break-up at $\varepsilon = 3.52^{+}$. These instabilities can be attributed to the rapid increase in radial flow kinematics and high extension-rates generated at the filament mid-plane, which differ from the imposed constant extension-rates. This is held to be physically acceptable, as discussed later.

For an ideal uniaxial flow, the radial and axial velocity profiles can be obtained from equation (11). For flows, which are not purely uniaxial, Spiegelberg *et al.* (1996) proposed a lubrication theory solution (referred to as analytical) for viscous Newtonian fluids. This approximation is true for small Hencky-strain levels. Hence, we have compared our computed radial and axial velocity profiles with this solution, described by

$$U_r = -3\dot{\varepsilon}_0\left(1 - \frac{z}{L_\mathrm{p}}\right)\left(\frac{z}{L_\mathrm{p}}\right), \tag{28}$$

$$U_z = -\dot{L}_p r\left(3 - 2\frac{z}{L_\mathrm{p}}\right)\left(\frac{z}{L_\mathrm{p}}\right)^2. \tag{29}$$

The comparison of the complete numerical solution with that represented by equations (28) and (29) demonstrates the accuracy of radial and axial velocity profiles at the low Hencky-strains (Figures 10-13). Axial velocity profiles are calculated along the centreline ($r = 0$) and the radial velocity profiles, U_r, on the deformed free-surface. On mesh Ml, our results are in close proximity with the analytical solution (lubrication approximation) (Spiegelberg *et al.*, 1996) up to Hencky-strains $\varepsilon = 2.56^{+}$. After this stage, slight deviation is detected, see

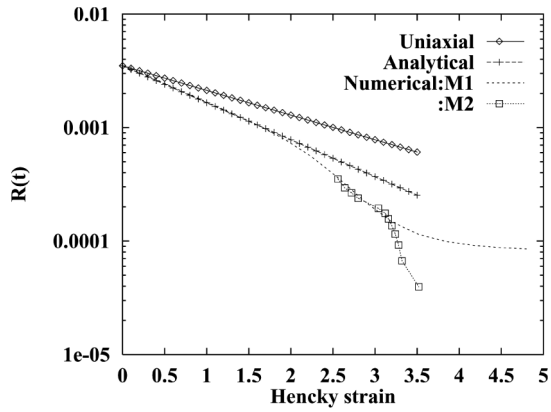

Figure 9.
Minimum filament radius, $R_{\min}(\varepsilon)$, on symmetry mid-plane ($z = 0$), mesh M1 (ε = 0-2.56): 12 × 40 elements, 2,025 nodes; mesh M2 ($\varepsilon = 2.56^{+}$-3.52) : l2 × 106 elements, 5,025 nodes

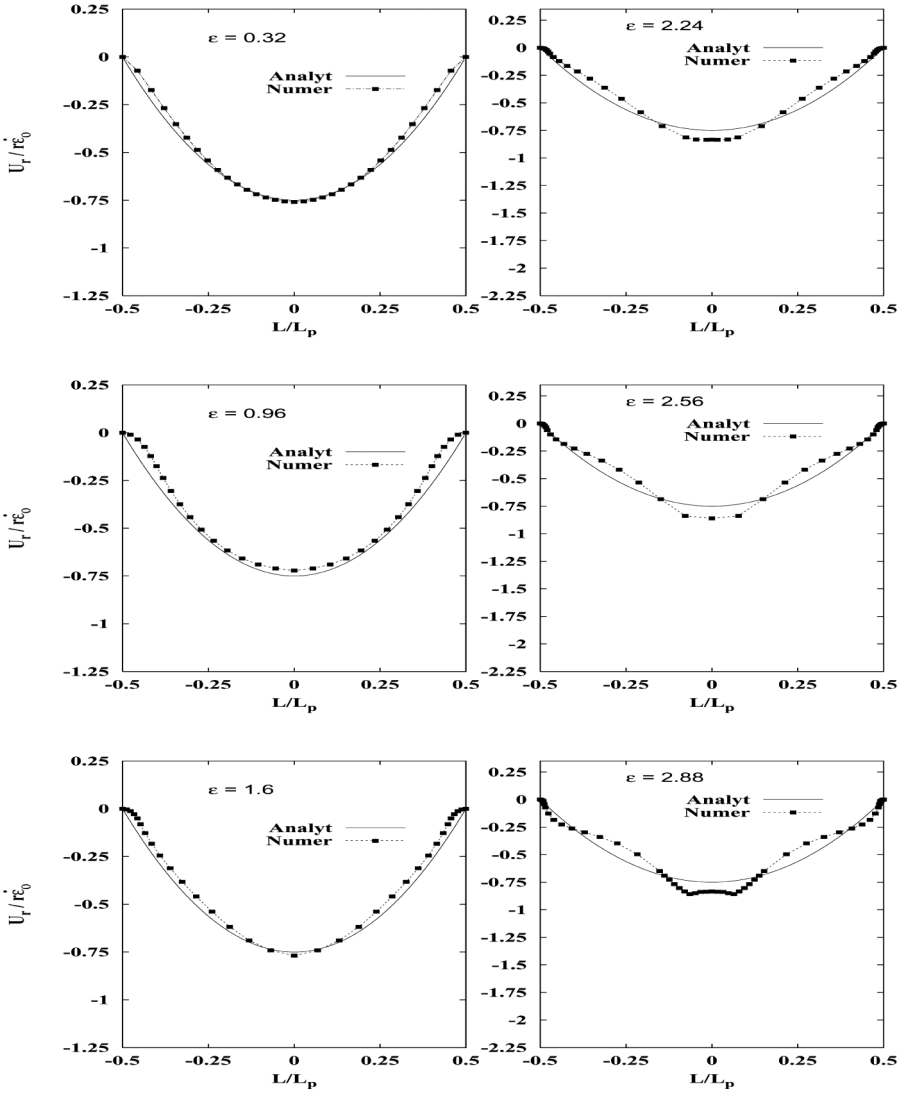

Figure 10.
U_r profiles, along free-surface, mesh M1, ($\varepsilon = 0.32, 0.96, 1.6, 2.24, 2.56, 2.88$)

Figure 12 for $\varepsilon = 2.88$. With the new mesh M2, we have been able to recapture the field solution accuracy up to Hencky-strain level of $\varepsilon = 3.52$, when radial velocity peaks dramatically at the filament mid-plane. Such a scenario leads to the ultimate thinning and break-up of the liquid-bridge (Figures 11 and 14). Large radial displacements are observed at the mid-symmetry plane, due to the peak in the radial velocity in that region. Colour contours of both the radial and axial velocity components are shown in Figures 14 and 15, respectively. Parabolic profiles of radial velocity component are obtained throughout the

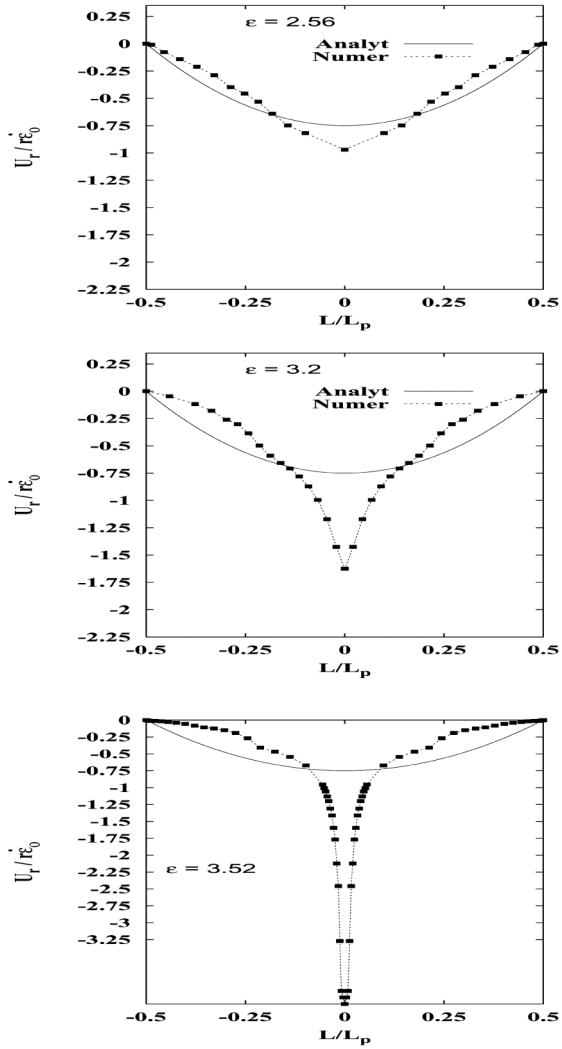

Figure 11.
U_r profiles along free-surface, mesh M2, ($\varepsilon = 2.56, 3.2, 3.52$)

liquid bridge. The axial velocity component has exposed uniformity across the filament and non-homogeneity along the length of the liquid-bridge, maxima on the plate, whilst vanishing on the mid-symmetry plane. The radial velocity [4] is observed to be the major driving factor. It is responsible for the generation of the correct free-surface profile (curvature/location), and assists in retaining the solution accuracy and stability up to large Hencky-strain levels. Our results on filament curvature (shape) are in close agreement with those of Yao and McKinley (1998) (who have enforced velocity compensation) up to Hencky-strain levels of 3.0 units, and with Sizaire and Legat (1997) up to Hencky-strain levels of $\varepsilon = 2.0^{+}$ units (Figure 9).

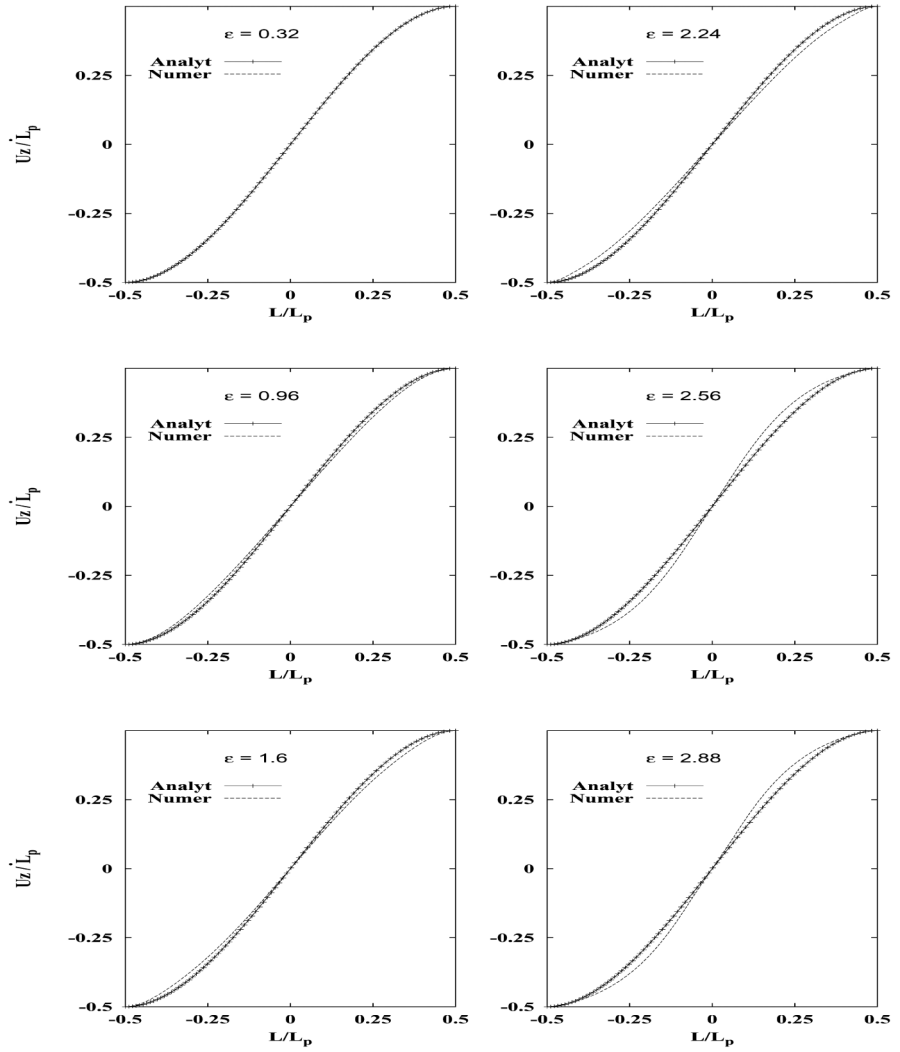

Figure 12.
U_z profiles, centreline ($r = 0, z$), mesh M1, ($\varepsilon = 0.32, 0.96, 1.6, 2.24, 2.56, 2.88$)

Another important quantity, difficult to estimate experimentally, is the history of the rate-of-deformation within the liquid bridge. In an ideal uniaxial flow, the rate-of-deformation tensor satisfies equation (11) at all times. Thus, a shear-free flow field is obtained, as $D_{rz} = 0$ and $D_{zz} = \dot{\varepsilon}_0$. The flow under consideration inherits a shearing component due to the no-slip boundary conditions at the end-plates. The colour contours of D_{rz} and D_{zz} components of the rate-of-deformation tensor are shown in Figures 16-17. Initially (at small Hencky-strains), the flow in the liquid-bridge is dominated by its radial velocity component (moving inward). Consequently, some shear may be attributed to

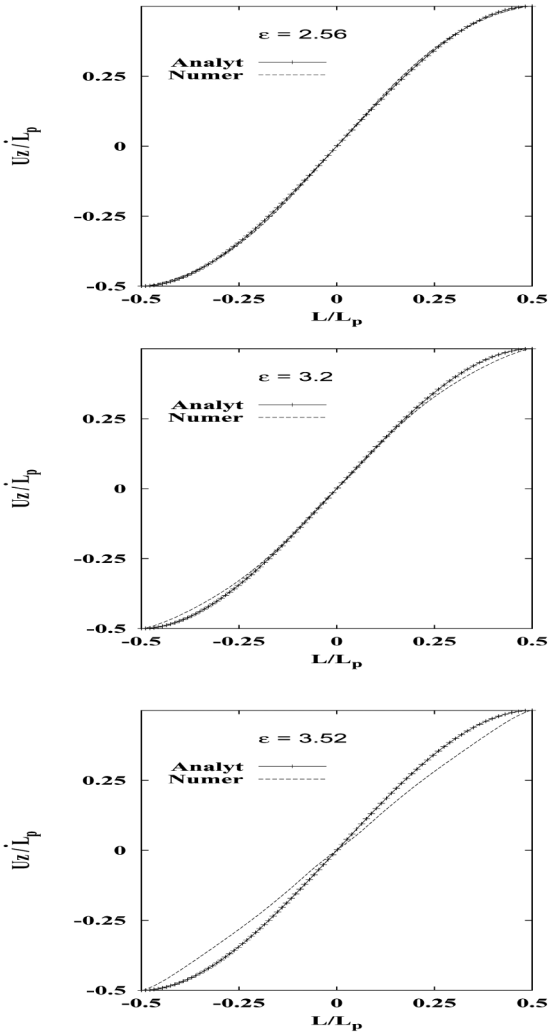

Figure 13.
U_z, centerline ($r = 0, z$), mesh M2, ($\varepsilon = 2.56, 3.2, 3.52$)

the underpinning boundary conditions, prior to the development of dominant extension in the flow. Hence, significant shearing effects can be observed at small Hencky-strain levels of $\varepsilon = 0.32$. Maxima in D_{rz} is localised to the interface of the free-surface and the rigid end-plate. These shearing effects decline with increasing Hencky-strain levels (Figure 16). Equivalently, maxima in D_{zz} are observed at the mid-plane.

Sizaire and Legat (1997) reported stability in their numerical simulations up to Hencky-strains of 4.5^{+} for Newtonian flows. Nevertheless, these authors fail to report explicitly on accuracy attainment in field solution, providing only scalar measures such as line-plots. From these line-plots, it would appear that

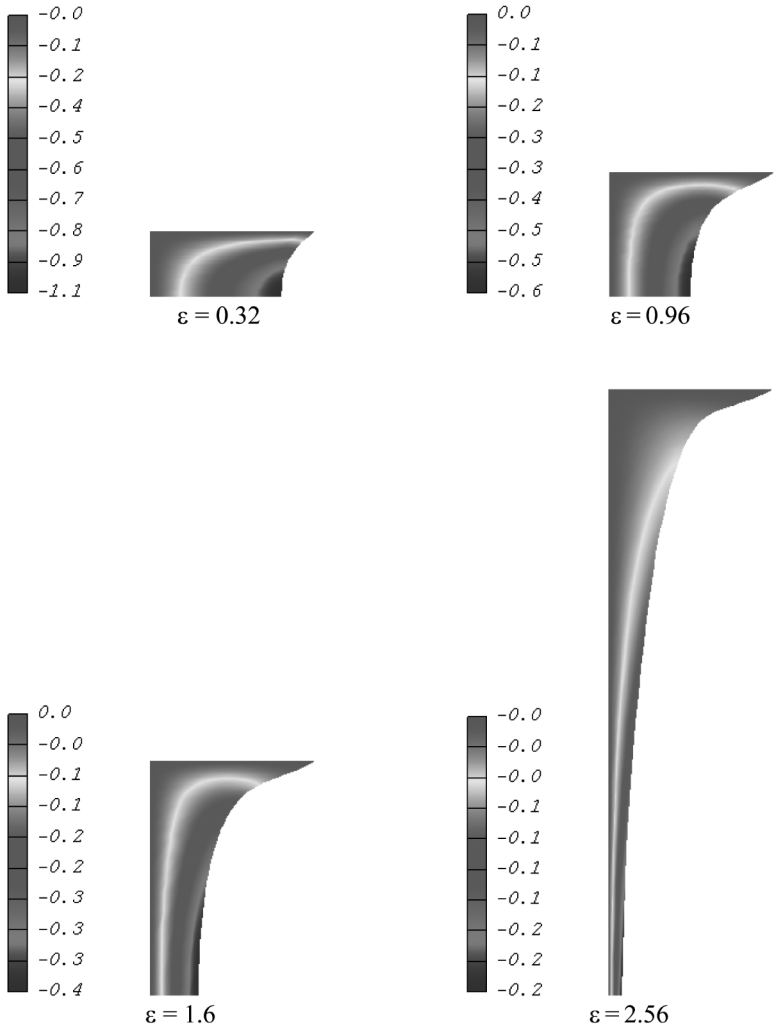

Figure 14.
U_r colour contours, various Hencky-strains (times)

their solutions capture accuracy at low Hencky-strain levels. Deformation field measures are not discussed. To avoid mesh distortion and retain smoothness, these authors utilised a Thompson elliptic-operator remeshing technique. A similar approach was adopted by Yao and McKinley (1998), with recourse to velocity compensation. In this manner, Yao and McKinley reached large Hencky-strains of 4.8^{+} Nonetheless, in a recent paper, Gaudet and McKinley (1996) investigated a conventional approach, coupled to a velocity compensation technique, for both Newtonian and non-Newtonian viscoelastic flows. Notably, the numerical simulations of Gaudet and McKinley diverged beyond Hencky-strains of 2.8^{+}. *The cause of this failure was not identified.*

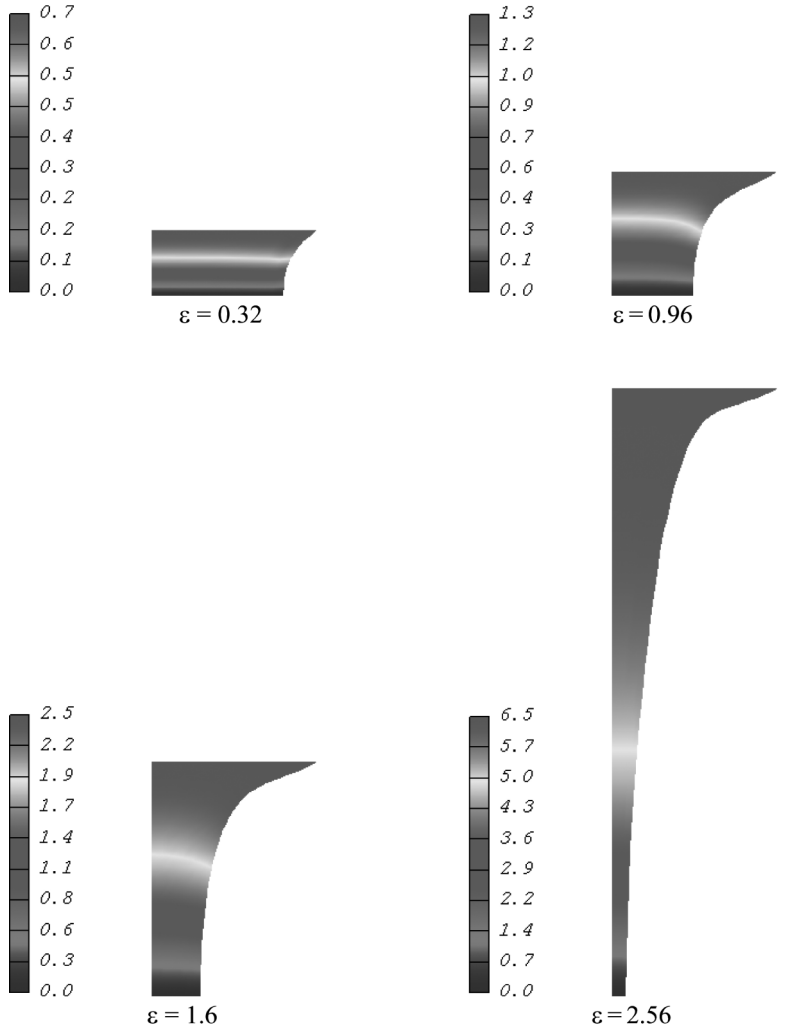

Figure 15.
U_z colour contours, various Hencky-strains (times)

Here, both accuracy and stability were gathered up to filament-breakup. In the light of our current findings, we speculate that the likely cause of such premature numerical divergence is due to the excessive mesh aspect-ratios. Settling upon an appropriate mesh aspect-ratio may suppress such numerical shortcomings.

Figure 9 shows that the minimum filament radius, $R_{\min}(t)$, beyond the Hencky-strain levels of $\varepsilon = 2.0$, decreases in a complicated fashion. Strain-rates vary both in space and time. Consequently, analysis of results becomes complicated, which detracts from accurate determination of material properties (Tirtaatmadja and Sridhar, 1993). Since the flow near the mid-plane

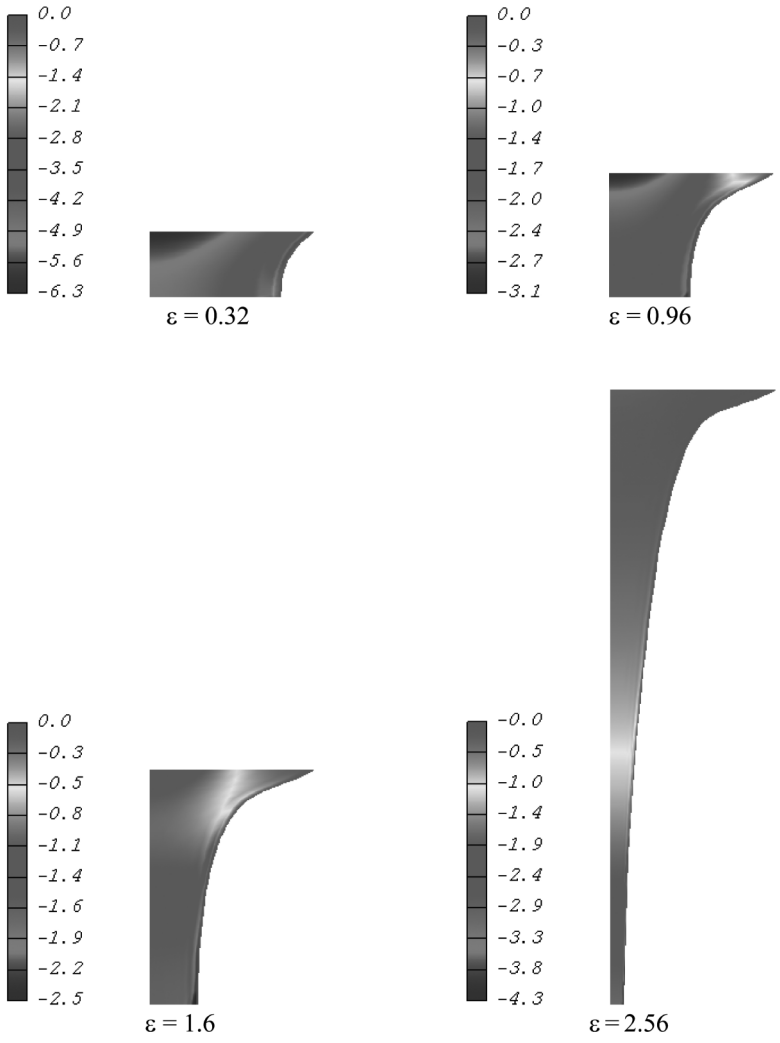

Figure 16.
Deformation-rate colour contours: shear component D_{rz}, various Hencky-strains (times)

is almost shear-free, Kröger *et al.* (1992) and Spiegelberg *et al.* (1996) proposed a method to compute, transient extensional viscosity, based on an effective deformation-rate:

$$\dot{\varepsilon}_{\text{eff}}(t) = -\frac{2}{R_{\text{mid}}}\frac{\mathrm{d}R_{\text{mid}}}{\mathrm{d}t} = \frac{-2U_{r,\text{mid}}}{R_{\text{mid}}}. \tag{30}$$

In addition and for comparison purposes, we have computed both the average and pointwise estimates of deformation-rates at the filament mid-plane, following Yao and McKinley (1998), viz.:

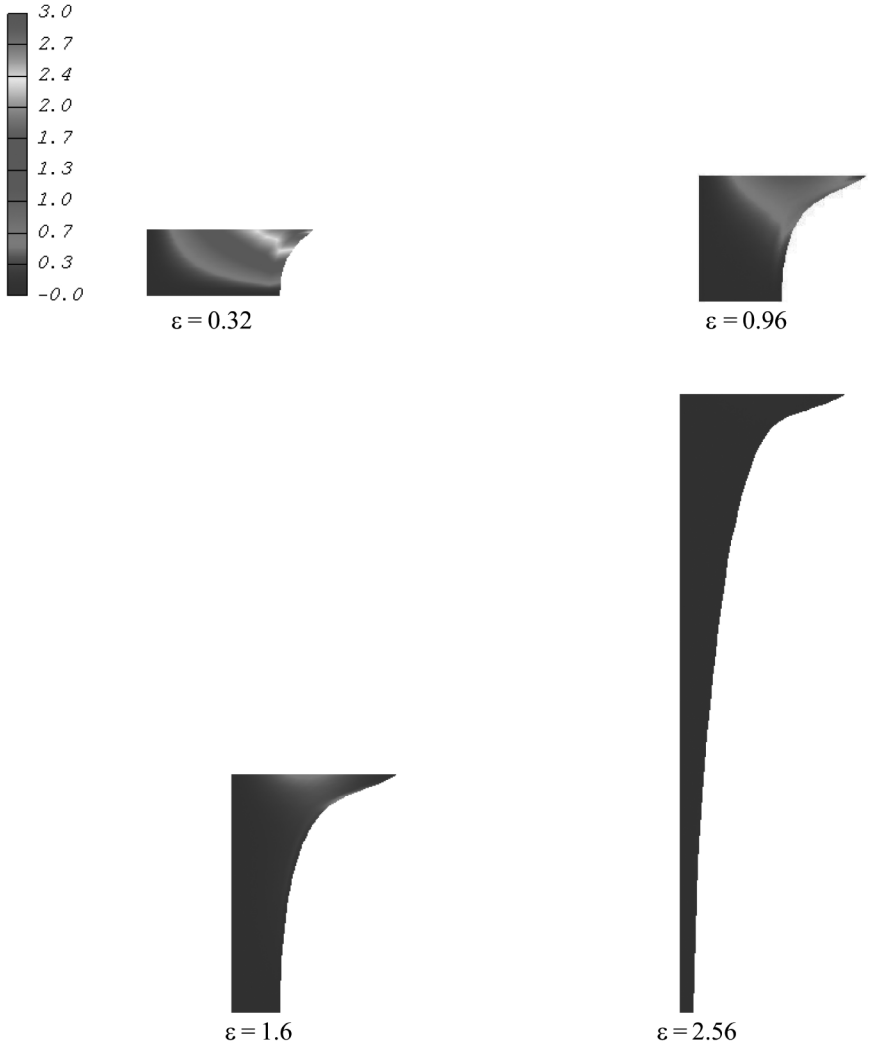

Figure 17.
Deformation-rate colour contours: axial component D_{zz}, various Hencky-strains (times)

(1) average axial velocity gradient over filament mid-plane

$$\dot{\varepsilon}_{\text{ave}}(t) = 2\int_0^{R_{\text{mid}}} rD_{zz}[r, z = 0]\mathrm{d}r/R_{\text{mid}}^2, \tag{31}$$

(2) pointwise value of D_{zz} at filament central-point (0, 0)

$$\dot{\varepsilon}_{\text{point}}(t) = D_{zz}[r = 0, z = 0]. \tag{32}$$

Deformation-rates calculated using equations (30) and (32) provide identical profiles (Figure 18). A slight, but consistent overestimation is observed through the averaged evaluation of equation (31). Both $\dot{\varepsilon}_{\text{point}}(t)$ and $\dot{\varepsilon}_{\text{eff}}(t)$ are consistent with the lubrication prediction, $\dot{\varepsilon}_{\text{eff}}(t) = 1.5\dot{\varepsilon}_0$ (Spiegelberg *et al.*, 1996). A constant extension-rate is maintained up to Hencky-strain levels of $\varepsilon = 3.3$ units. These results are in close agreement with those of Sizaire and Legat (1997) up to higher Hencky-strain levels. Moreover, in our numerical simulations, we have been able to recover the imposed strain-rate without recourse to *velocity compensation*.

Following Yao and McKinley (1998), in the absence of inertia and gravity, we have modified equation (17) to a generalized form to compute the transient

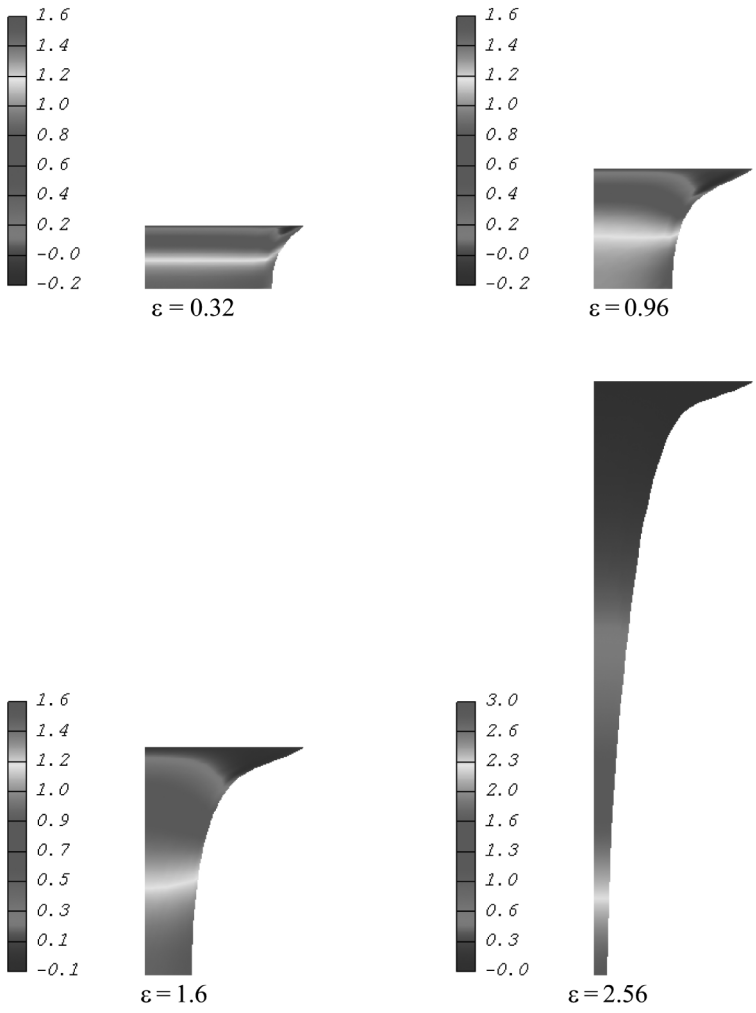

Figure 18.
Extension-rate development versus Hencky-strain (pointwise: $r = 0, z = 0$; effective: $R_{\text{mid}}(t)$, $z = 0$; average: r, $z = 0$); line-points (at constant unity) indicate initial imposed stretch-rate $\dot{\varepsilon}_0$, non-dimensional)

Trouton ratio as:

$$\mathrm{Tr} = \frac{\mu_e}{\mu_0} = \frac{F_z}{\mu_0 \dot{\varepsilon}_0 \pi R_{\mathrm{mid}}^2} - \frac{\chi}{\mu_0 \dot{\varepsilon}_0 R} \tag{33}$$

where R_{mid} is the minimum radius at the mid-plane of the filament and χ is the surface tension coefficient. The normal force F_z on the plate is evaluated as:

$$F_z(t) = \int_A [\tau_{zz}(r, z_0, t) + P_0] \, \mathrm{d}A \tag{34}$$

where the range of integration, A, is the domain of the circular filament-foot (radius R) on the end-plate at $z_0 = 0$. Due to the no-slip boundary conditions on the moving end-plate, employing the continuity equation and equation (14), we gather that both axial and radial normal stress components must vanish. Hence, for Newtonian flows and equation (34), the pressure is the only non-trivial quantity that contributes to the normal force on the moving end-plates. Pressure colour contours are displayed in Figure 19. Maxima in pressure magnitude arises on the plate at small Hencky-strains. With increasing Hencky-strains, the location of maxima in pressure magnitude switches to the symmetry mid-plane and vanishes on the rigid-end plate. Consequently, the force measured on the moving end-plate decreases and vanishes with time (Figure 20). The computed normal force N_f, on the plate is negated, to imply physical meaning through magnitude. The transient evolution profile of Tr is shown in Figure 21. The curve of Tr based on $\dot{\varepsilon}_{\mathrm{point}}(t)$ and $\dot{\varepsilon}_{\mathrm{eff}}(t)$ asymptotes to the Newtonian value of $\mathrm{Tr} = 3$, up to Hencky-strain levels of 2.56, concurring with the literature (Sizaire and Legat, 1997; Yao and McKinley, 1998).

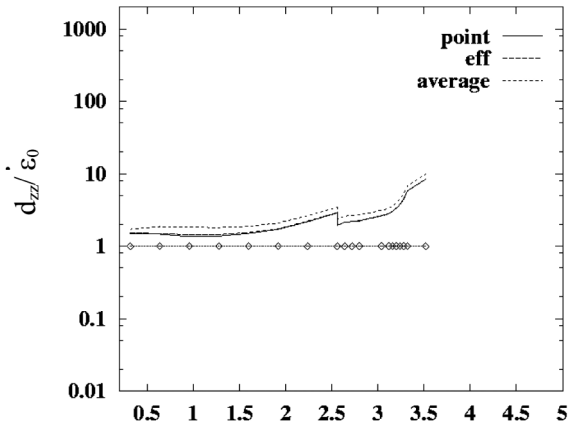

Figure 19.
Pressure colour contours, various Hencky-strains (times)

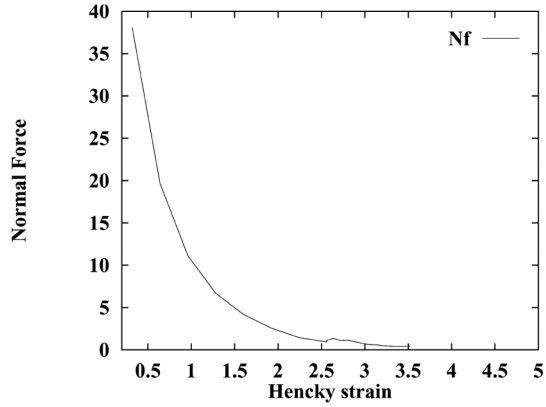

Figure 20.
Normal force, N_f, on moving-plate versus Hencky-strain (non dimensional)

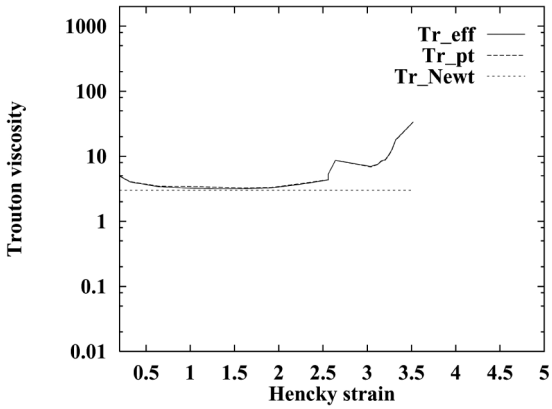

Figure 21.
Tr development versus Hencky-strain, symmetry mid plane $(r, z = 0)$

8. Conclusions

Here, our main attention has been focused on investigating new algorithmic aspects in the context of applying a Taylor-Galerkin/pressure-correction scheme to the filament stretching problem. This has provided insight into the onset of instabilities, which cause solution degradation and ultimately leads to filament break-up. Our results have shown that a suitable choice of mesh aspect-ratio around the filament mid-plane region, where break-up occurs, is particularly important. This can capture accuracy and retain stability up to large Hencky-strain levels. In this sense, we have shown that an appropriate choice of remeshing technique plays a crucial role in achieving the solution stability and accuracy. We summarise the achievements borne out through the present study as:

- successful implementation of a TGPC scheme (SITpak), for a true-transient flow, under the presence of an evolving free-surface;

- proposal of an effective, low-cost remeshing algorithm;
- circumvention of the need for correction via velocity compensation;
- attainment of filament stability up to the large Hencky-strain levels of $\varepsilon = 4.8^{+}$; and
- capture of field accuracy up to impressive Hencky-strain levels of $\varepsilon = 3.52^{+}$. Here, our results are highly competitive.

The present approach is based on direct evaluation from the kinematics and extension rates involved. Hence, it departs from the velocity compensation approach, as employed in Yao and McKinley (1998). A triangular-based finite element approach is applied here, and the results obtained are consistent with those appearing in the literature (Sizaire and Legat, 1997; Yao and McKinley, 1998) on filament shape and in field representation, where equitable. Our numerical results bear out that radial profiles vary non-uniformly along the liquid bridge and reach a minimum, $R_{\min}$, at the mid-point of the filament. This is due to the underpinning boundary conditions at the interface between the rigid non-deformable moving end-plates and the free-surface. The early evolution of $R_{\min}$ decreases smoothly according to the analytical (lubrication) approximation (Spiegelberg *et al.*, 1996). Subsequently, slight departure is observed: the slope changes gradually and becomes steeper, just prior to the filament break-up. The predicted velocity profiles, radial component U_r along the free-surface and axial U_z along the axial centreline, track the lubrication approximation up to Hencky-strain levels of $\varepsilon = 3.0$ units.

In terms of our sampled field results on rate-of-deformation at specific Hencky-strain levels, the flow is observed to experience some shearing effects at low Hencky-strains. These subsequently diminish with increasing Hencky-strains. The presence of these shearing effects indicates that the flow is not purely uniaxial, and particularly so at low Hencky-strains. This state of affairs will be reflected in laboratory experiments and the measurement of material properties through filament stretching rheometers. Gaudet and McKinley (1998), Sizaire and Legat (1997), Yao and McKinley (1998) and Yao *et al.* (1998) have all reported similar findings. Both effective extension-rates and resultant Trouton ratios are in close agreement with the literature (Sizaire and Legat, 1997; Yao and McKinley, 1998). Future work will be devoted in investigating the consequences of adaptive remeshing algorithms, application of velocity compensation, or a combination of both.

Notes

1. Similar to the approach adopted by Wilkes *et al.* (1999), with reference to dynamic drop formation. Note that in the current context, volume conservation is vital, determining field solution and correct surface curvature.
2. A remeshing strategy with the ability to maintain element density (concentration) and mesh aspect ratio, near the point or line of reference, without adding/removing elements.

3. Appeals to underlying fe-interpolants, but at selected sample points and along restricted directions.
4. Free-surface movement largely depends on U_r. The larger the U_r (magnitude), the smaller the $R_{\text{mid}}(t)$. Hence, the larger the effective deformation-rate and Trouton ratio.

References

Ainser, A., Carrot, C., Guillet, J. and Sirakov, I. (2000), "Transient viscoelastic analysis of falling weight experiment", *XIIIth Int. Cong. Rheol.*, Cambridge, UK, Vol. 2, pp. 259-61.

Barnes, H.A., Hutton, J.F. and Walters, K. (1989), *An Introduction to Rheology*, Elsevier, Amsterdam.

Berg, S., Kröger, R. and Rath, H.J. (1995), "Measurement of extensional viscosity by stretching large liquid bridges in microgravity", *J. Non-Newt. Fluid Mech.*, Vol. 55, pp. 307-19.

Frederiksen, C.S. and Watts, A.M. (1981), "Finite element method for time-dependent incompressible free surface flow", *J. Comp. Phys.*, Vol. 39, pp. 282-304.

Gaudet, S. and McKinley, G.H. (1996), "Extensional deformation of Newtonian liquid bridges", *Phys. Fluids*, Vol. 8, pp. 2568-79.

Gaudet, S. and McKinley, G.H. (1998), "Extensional deformation of non-Newtonian liquid bridges", *Comp. Mechs.*, Vol. 22, pp. 461-76.

Hassager, O., Kolte, M.I. and Renardy, M. (1998), "Failure and non-failure of fluid filaments in extension", *J. Non-Newt. Fluid Mech.*, Vol. 76, pp. 137-51.

Hawken, D.M., Tamaddon-Jahromi, H.R., Townsend, P. and Webster, M.F. (1990), "A Taylor-Galerkin based algorithm for viscous incompressible flow", *Int. J. Num. Meth. Fluids*, Vol. 10, pp. 327-51.

Keunings, R. (1986), "An algorithm for the simulation of transient viscoelastic flows with free surfaces", *J. Comp. Phys.*, Vol. 62, pp. 199-220.

Khan, S.A. and Larson, R.G. (1987), "Comparison of simple constitutive equations for polymer melts in shear and biaxial and uniaxial extensions", *J. Rheol.*, Vol. 31, pp. 207-34.

Kolte, M.I. and Szabo, P. (1999), "Capillary thinning of polymeric filaments", *J. Rheol.*, Vol. 43, pp. 609-25.

Kröger, R., Berg, S., Delgado, A. and Rath, H.J. (1992), "A stretching behaviour of large polymeric and Newtonian liquid bridges in plateau simulation", *J. Non-Newt. Fluid Mech.*, Vol. 45, pp. 385-400.

Matta, J.E. and Tytus, R.P. (1990), "Liquid stretching using a falling cylinder", *J. Non-Newt. Fluid Mech.*, Vol. 35, pp. 215-29.

Matallah, H., (1998), PhD thesis, University of Wales Swansea, Swansea, UK.

Padmanabhan, M. (1995), "Measurement of extensional viscosity of viscoelastic liquid foods", *J. Food Eng.*, Vol. 25, pp. 311-27.

Sizaire, R. and Legat, V. (1997), "Finite element simulation of a filament stretching extensional rheometer", *J. Non-Newt. Fluid Mech.*, Vol. 71, pp. 89-107.

Spiegelberg, S.H. and McKinley, G.H. (1996), "Stress relaxation and elastic decohesion of viscoelastic polymer solutions in extensional flow", *J. Non-Newt. Fluid Mech.*, Vol. 67, pp. 49-76.

Spiegelberg, S.H., Ables, D.C. and McKinley, G.H. (1996), "The role of end-effects on measurements of extensional viscosity in filament stretching rheometers", *J. Non-Newt. Fluid Mech.*, Vol. 64, pp. 229-67.

Tanguy, P., Fortin, M. and Choplan, L. (1984), "Finite element simulation of dip coating, I: Newtonian fluids", *Int. J. Num. Meth. Fluids*, Vol. 4, pp. 441-57.

Thompson, J.F., Warsi, Z.U.A. and Mastion, C.W. (1985), *Numerical Grid Generation: Foundation and Applications*, North-Holland, Amsterdam.

Tirtaatmadja, V. and Sridhar, T. (1993), "A filament stretching device for measurement of extensional viscosity", *J. Rheol.*, Vol. 37, pp. 1081-1102.

Tirtaatmadja, V. and Sridhar, T. (1995), "Comparison of constitutive equations for polymer solutions in uniaxial extension", *J. Rheol.*, Vol. 39, pp. 1133-60.

Townsend, P. and Webster, M.F. (1987), "An algorithm for the three-dimensional transient simulation of non-Newtonian fluid flows", *Proc. NUMETA 87*, Martinus Nijhoff, Publishers, Dordrecht, Vol. 2.

Tripathi, A., Whittingstall, P. and McKinley, G.H. (2000), "Using filament stretching rheometry to predict strand formation and 'processability' in adhesive and other non-Newtonian fluids", *Rheol. Acta.*, Vol. 39, pp. 321-37.

Wilkes, E.D., Philips, S.D. and Basaran, O.A. (1999), "Computational and experimental analysis of dynamics of drop formation", *Phys. Fluids*, Vol. 11 No. 12, pp. 3577-98.

Yao, M. and McKinley, G.H. (1998), "Numerical simulation of extensional deformations of viscoelastic liquid bridges in filament stretching devices", *J. Non-Newt. Fluid Mech.*, Vol. 74, pp. 47-88.

Yao, M., McKinley, G.H. and Debbaut, B. (1998), "Extensional deformation, stress relaxation and necking failure of viscoelastic filaments", *J. Non-Newt. Fluid Mech.*, Vol. 79, pp. 469-501.

Further reading

Gresho, P.M. and Sani, R.L. (1998), "Incompressible flow and the finite element methods: advection-diffusion and isothermal flows", Vol. 1, Wiley, New York.